# Forced convection past a circular cylinder in a planar Poiseuille flow

C.A. Klettner

[a]University College London, , London, WC1E 7JE, , United Kingdom

**Abstract**

In this work the transfer of a passive scalar (temperature) from a circular cylinder (radius $R$) in a planar Poiseuille flow (height $2h$) is investigated with numerical simulations. The study varies the channel half-height to cylinder radius $\epsilon = h/R$, the inertial parameter $\Lambda = (U_c R/\nu)(h/R)^2$ and the Péclet number $Pe = U_c R/\alpha$, where $U_c$ is the midplane velocity, $\nu$ is the kinematic viscosity and $\alpha$ is the thermal diffusivity. There has been significant amount of work for $\epsilon \gg 1$, therefore this work will focus on the range, $0.03 \leq \epsilon \leq 1$, which has been chosen to show the effect of geometry and inertia on the flow features and the subsequent transfer. As $\epsilon$ is decreased the Nusselt number increases and this behaviour is explained with velocity and temperature profiles.

Particularly for $\epsilon = 0.03$, the local Nusselt number has a significant vertical variation (in the $z$-direction) when $\Lambda$ and $Pe$ are increased past certain values. For $\Lambda \ll 1$ and $Pe > 10^3$ this is due to the non-uniform incident flow present in the Hele-Shaw cell while for $\Lambda = O(1)$, it is the secondary flow that is induced at the sides of the cylinder. For these latter flows the transfer in the midplane is reduced relative to near the side walls, due to the triple turning point radial velocity profile adjacent to the circular cylinder. For $\Lambda \leq 1$, the Nusselt number is only a function of $Pe$. However, for $\Lambda > 1$, the secondary flow results in a slightly increased Nusselt number.

*Keywords:* Forced convection, Hele-Shaw flow

**Nomenclature**

General symbols

| | |
|---|---|
| $G$ | Far-field pressure gradient |
| $h$ | Half-height of the channel |
| $L$ | Length of domain |
| $L_v$ | Length of midplane recirculation region |
| $Nu$ | Global Nusselt number |
| $Nu_\theta$ | Local Nusselt number |
| $p$ | Non-dimensional fluid pressure |
| $\tilde{p}$ | Dimensional fluid pressure |
| $Pe$ | Péclet number based on $U_c$ and on cylinder radius $R$ |
| $\bar{Pe}$ | Péclet number based on $\bar{U}$ and cylinder diameter $2R$ |
| $Pr$ | Prandtl number |
| $R$ | Cylinder Radius |
| $\bar{Re}$ | Reynolds number based on $\bar{U}$ and cylinder diameter $2R$ |
| $r$ | Non-dimensional radial coordinate |
| $T$ | Non-dimensional fluid temperature |
| $\tilde{T}$ | Dimensional fluid temperature |
| $\boldsymbol{u} = \{u, v, w\}$ | Non-dimensional fluid velocity |
| $\tilde{\boldsymbol{u}}$ | Dimensional fluid velocity |
| $U_c$ | Channel centreline velocity |
| $\bar{U}$ | Average channel horizontal velocity |
| $u_\theta$ | Dimensionless tangential velocity |
| $u_r$ | Dimensionless radial velocity |
| $W$ | Width of domain |
| $\boldsymbol{x} = \{x, y, z\}$ | Non-dimensional Cartesian coordinate |
| $\tilde{\boldsymbol{x}}$ | Dimensional Cartesian coordinate |

Greek Symbols

| | |
|---|---|
| $\alpha$ | Fluid thermal diffusivity |
| $\Delta_r, \Delta_z, \Delta_\theta$ | Mesh size in the respective direction |
| $\delta_g$ | Geometric boundary layer thickness |
| $\delta_\alpha$ | Thermal boundary layer thickness |
| $\epsilon$ | Ratio of half-height of the channel to radius |
| $\theta$ | Azimuthal coordinate |
| $\theta_v$ | Midplane separation angle |
| $\Lambda$ | Inertial parameter |
| $\mu$ | Fluid dynamic viscosity |
| $\nu$ | Fluid kinematic viscosity |

$\rho$ Fluid density

Subscripts

$\infty$ Value at inlet

$S$ Value at cylinder surface

Superscripts

$*$ Stretched coordinate system

## 1. Introduction

Motivated by a variety of applications including heat exchangers and coastal vegetation there have been many studies on forced convection past single cylinders (Nakamura *et al.* 2004), tandem cylinders (Mahir & Altac 2014) and multiple cylinders grouped in an array (Klettner 2020). For vertically and laterally unbounded forced convection past bluff bodies many correlations have been proposed which usually correlate the Nusselt number with the Reynolds number and the Prandtl number (*e.g.* Knudsen & Katz 1958; Churchill & Bernstein 1977). These correlations usually scale with approximately the square root of the Reynolds number to reflect the thinning of the boundary layer thickness with an increase in the Reynolds number (Batchelor 1967). For low Reynolds number steady flows, Dennis *et al.* (1968) investigated the two-dimensional heat transfer from a cylinder using the Oseen equations for the fluid flow.

There has been a significant amount of research on the flow past a confined cylinder due to its relevance in microfluidics mixing (Zhang *et al.* 2019) and as forced convection is the dominant form of cooling in these applications (Renfer *et al.* 2013). When $\epsilon \approx 1$ there will be a non-uniform incident Poiseuille flow where the confinement can have a significant affect on the flow characteristics. For example vortex shedding can be suppressed when the confinement and/or Reynolds number is sufficiently small (Zhang *et al.* 2019). The effect of these geometric and flow conditions was only studied hydrodynamically; the effect on the transfer was not considered.

When $\epsilon \ll 1$ and the inertial parameter $\Lambda \ll 1$ vertical confinement results in the presence of a geometric boundary layer that is confined to adjacent to the cylinder surface (with a radial extent of $O(h)$), (Thompson 1968; Guglielmini *et al.* 2011). When $\Lambda > O(\epsilon)$, a secondary flow is induced adjacent to the cylinder on the windward side. As the inertial parameter is further increased to $O(1)$ this boundary layer thickness remains relatively constant (Klettner & Smith 2022). For this physical set up the Prandtl number is not instructive in determining the ratio of the thermal and momentum thicknesses, as is usually the case for inviscid/viscous boundary layers in unbounded flows, which makes the correlations above not appropriate for these geometric conditions.

Gorin *et al.* (1995) performed laboratory experiments and theoretical work for the mass transfer from a circular cylinder (with $\epsilon = 0.031$). $\Lambda$ and the Péclet number where simultaneously increased and were compared to an analytical solution to a simplified depth-averaged convection-diffusion equation. Investigation of the vertical variation of flux from the cylinder surface was not possible in the experiments or the theoretical analysis.

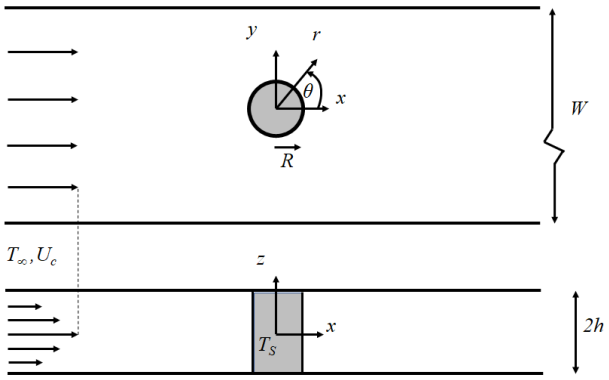


Figure 1: Schematic of planar Poiseuille flow (with maximum velocity $U_c$) past a cylinder (radius $R$), highlighted in grey, between two flat plates separated by a distance $2h$. The origin for the Cartesian and cylindrical polar coordinate system is the cylinder centre in the midplane. The span $W$ is taken to be very large in this study. The temperature of the incident flow is $T_\infty = 0$ while on the cylinder surface $T_S = 1$. Note that in the top figure, $\hat{\mathbf{z}}$ is pointing out of the page and in the bottom figure $\hat{\mathbf{y}}$ is pointing into the figure. Figure modified from Klettner & Smith (2022).

Choi *et al.* (2006) used conformal mapping techniques and numerical methods to investigate the absorption of a passive scalar in two-dimensional potential flows. The flux from the cylinder surface and the wake were studied in detail. In the wake, two regimes were identified namely, a 'diffusive' cloud for low Péclet number and a narrow wake as the Péclet number was increased above 60. The importance of this was discussed in the context of coating fibres in a gas flow. A further application of this set up can be found in the dissolution of a body in the steady flow of a Hele Shaw cell (Ladd *et al.* 2020), which can be used as a prototype for reactive transport at the pore scale. Here, the reaction is treated constant across the cross section which is appropriate if the reaction time is small. However there might be flow situations when this assumption is not appropriate and a vertical variation in the dissolution (due to the vertical variation in the transfer) might be important.

As can be seen from the literature there is a significant amount work on the forced convection past cylinders. The gap in the literature is a study of the flow features and subsequent transfer when $\epsilon \leq 1$. Therefore the purpose of this work is to study the forced convection past a circular cylinder for $\epsilon \leq 1$ and varying $\Lambda$ and the Péclet number. Three-dimensional numerical simulations allow the study all aspects of this problem including the vertical variation of the thermal transfer. The paper is organised as follows; the problem and governing equations and diagnostics are presented in §2. The numerical methods are reviewed in §3. Numerical results are presented in §4 and §5 and conclusions are given §6.

## 2. Problem definition and governing equations

This section outlines the governing equations for flow and temperature in a confined channel (adapted from Klettner & Smith 2022). In this work we investigate the forced convection of a plane Poiseuille flow (with midplane velocity $U_c$) of a fluid (with a density and kinematic viscosity of $\rho$ and $\nu$ respectively) past a circular cylinder of radius $R$ (see figure 1). The midplane velocity is defined as $U_c = -Gh^2/(2\mu)$ where $\mu$ is the dynamic viscosity and $G$ is the far-field pressure gradient (which generates the plane Poiseuille flow), $h$ is half the gap height and $\epsilon = h/R$. The nondimensional governing equations for a steady, incompressible, Newtonian fluid are the continuity equation

$$\boldsymbol{\nabla} \cdot \boldsymbol{u} = 0, \tag{1}$$

the momentum equation

$$\Lambda(\boldsymbol{u} \cdot \boldsymbol{\nabla})\boldsymbol{u} = -\boldsymbol{\nabla} p + \epsilon^2 \boldsymbol{\nabla}^2 \boldsymbol{u}, \tag{2}$$

and the advection-diffusion equation for the temperature, $T$,

$$\boldsymbol{\nabla} \cdot (\boldsymbol{u} T) = \frac{1}{Pe} \boldsymbol{\nabla} \cdot (\boldsymbol{\nabla} T). \tag{3}$$

To non-dimensionalise the system the following variables have been used $\boldsymbol{u} = \tilde{\boldsymbol{u}}/U_c$, $\boldsymbol{x} = \tilde{\boldsymbol{x}}/R$ and $p = -2\tilde{p}/(GR) = \tilde{p}\Lambda/\rho U_c^2$. Here the inertial parameter is $\Lambda = (U_c R/\nu)(h/R)^2$ and the Péclet number is $Pe = U_c R/\alpha$ where $\alpha$ is the thermal diffusivity. To non-dimensionalise the temperature $T = (\tilde{T} - \tilde{T}_\infty)/(\tilde{T}_S - \tilde{T}_\infty)$ where $\tilde{T}_\infty$ and $\tilde{T}_S$ are the upstream and cylinder surface temperature respectively. Additionally to make comparisons with a uniform two-dimensional incident flow, a Reynolds number is defined as $\bar{Re} = 2\bar{U}R/\nu$ where $\bar{U} = U_c/1.5$ and an associated Péclet number $\bar{Pe} = \bar{Re}.Pr$, where the Prandtl number is $Pr = \nu/\alpha$.

In this work we will be considering heat transfer, however similar expressions can also be obtained in terms of mass transfer. In terms of thermal transfer, the local Nusselt number is defined as

$$Nu_\theta = \frac{2R}{(T_S - T_\infty)} \frac{\partial T}{\partial n}, \tag{4}$$

where $n$ is the normal into the surface of the cylinder and the associated Nusselt number is

$$Nu = \frac{1}{4\pi R h} \int_S Nu_\theta \mathrm{d}S, \tag{5}$$

where $S$ is the surface of the cylinder. To highlight flow features present in the geometric boundary layer adjacent to the circular cylinder (when $\epsilon \ll 1$), stretched coordinates are used, where $r^* = (r-1)/\epsilon$ where $r = \tilde{r}/R$ and $\boldsymbol{x}^* = \boldsymbol{x}/\epsilon$.

### 2.1. Choice of parameters

The governing equations highlight that the transfer from a cylinder will depend on the geometry ($\epsilon$), flow ($\Lambda$) and transfer ($Pe$) characteristics. This study will focus on $0.03 \leq \epsilon \leq 1$, as these display different flow features as $\Lambda$ is increased. We restrict the increase in $\Lambda$ such that all flows are steady (Tuckerman *et al.* 2014; Klettner & Smith 2022). In Section 4, air and water are studied for different Reynolds numbers (range $1.3 \leq \bar{Re} \leq 106.7$) and $0.25 \leq \epsilon \leq 1$. In Section 5, the confinement is fixed to $\epsilon = 0.03$ and the inertial parameter is varied in the range $0.001 < \Lambda < 5$ and The Péclet number is varied in the range of $1.1 < Pe < 1.1 \times 10^5$.

## 3. Numerical methods

Numerical simulations of (1-3) were carried out with the open-source computational fluid dynamics toolbox OpenFOAM using a finite-volume method (Weller *et al.* 1998). Three-dimensional structured meshes were generated in blockMesh. The flow-field and temperature solvers were *simpleFoam* and *scalarTransportFoam* respectively, which is appropriate for these steady, laminar flows. All schemes are second-order-accurate; the Gauss linear numerical scheme is used for the gradient and divergence operators for the velocity and pressure fields; the Gauss linear corrected numerical scheme is used for the diffusive terms while for temperature the Gauss linearUpwind scheme is used. Simulations are carried out until a convergence criteria of $10^{-6}$ is obtained.

The cylinder is placed in the middle of a domain of length $L = 200R$ and width $W = 100R$, such that the flow at the sides is not affected by the cylinder (a schematic of the set-up is shown in figure 1). The cylinder and the top and bottom plates have the no-slip condition applied, while the sidewalls have the no-flux condition. The inlet condition is that of Poiseuille flow (with the flow from left to right) and the outlet condition is $p = 0$. The temperature at the inlet and the cylinder are $T_\infty = 0$ and $T_S = 1$, respectively. A zero gradient boundary condition for the temperature is $\partial T/\partial z = 0$ at $z = \pm\epsilon$.

The finest mesh used for these calculations had a resolution in the vertical direction $\Delta_z/h = 2/71$ and radial direction $\Delta_r/h = 1/50$ (close to the cylinder), respectively. Detailed mesh independence and validation for the flow-field in a Poiseuille flow past a single cylinder and the transfer of a passive scalar in a uniform incident flow past a single cylinder (in a vertically unbounded flow) have been presented in Klettner & Smith (2022) and Klettner (2020), respectively. An additional mesh independence study for the transfer of a temperature past a circular cylinder in a Hele-Shaw cell is shown in the Appendix A.

## 4. Results for air and water for $0.25 \leq \epsilon \leq 1$

Due to their practical importance, in this section the thermal transfer and hydrodynamics for air and water, in the range of $0.25 \leq \epsilon \leq 1$ with varying Reynolds number is studied. In Figure 2 the present numerical simulations are compared to the correlation by Churchill and Bernstein (1977) and the two-dimensional numerical computations of Dennis *et al.* (1968). For reference, results for $\epsilon = 0.03$ are also shown (which will be the focus of the subsequent section). As anticipated, for similar flow conditions, the transfer is greater for water than air as

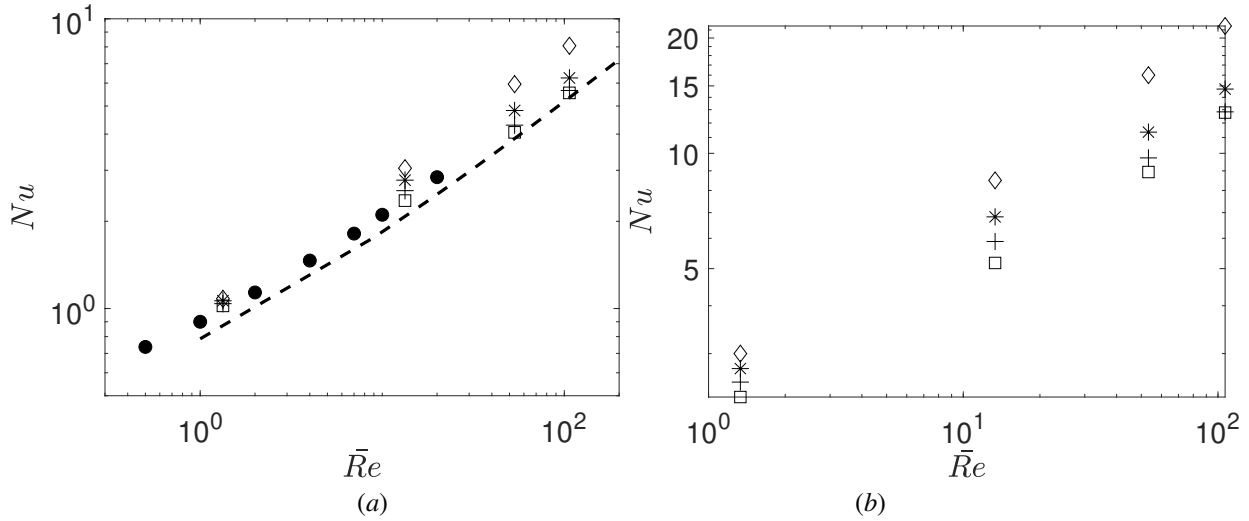


Figure 2: Variation of the Nusselt number with Reynolds number for (*a*) $Pr = 0.71$ and (*b*) $Pr = 6.9$. The current numerical simulations are shown for $\epsilon = 1$ (□), $\epsilon = 0.5$ (+), $\epsilon = 0.25$ (∗) and $\epsilon = 0.03$ (⋄). The filled symbols represent the two-dimensional simulations by Dennis *et al.* 1987 (•). The correlation by Churchill and Bernstein (1977) is shown as a dashed line. Note the difference in the ordinate scales.

the Prandtl number is an order of magnitude greater for water (Churchill & Bernstein 1977). It is evident that the correlation and also the two-dimensional results are quite different to the confined flow cases studied here, which is the focus of this section.

### *4.1. Variation with Re*

For both air and water, for a fixed $\epsilon$, the higher the Reynolds number the higher the Nusselt number. To investigate this further the azimuthal variation of the midplane local Nusselt number and contour plots of the midplane temperature for air and $\epsilon = 1$ for increasing Reynolds number are presented in figure 3. To show the vertical variation of the transfer, three lines are plotted in figure 3$(a, c, e)$, namely, the transfer close to the top wall (red lines), in the midplane (blue lines) and the average (dashed lines). This vertical variation in the local Nusselt number is due to the non-uniform incident flow on the cylinder, with higher transfer anticipated to be in the midplane as this is where the maximum velocity occurs.

Figure 3$(a, c, e)$ shows that for an increase in $\bar{Re}$, the local Nusselt number at the front of the cylinder ($\theta = \pi$) increases and scales approximately with $\bar{Pe}^{-1/3}$. This higher transfer for higher Reynolds numbers is due to the stagnation point flow; for higher Reynolds numbers the horizontal velocity is greater closer to the cylinder (with a steeper deceleration towards the front stagnation point) which leads to a thinner thermal boundary layer and an associated higher transfer (see figure 4*a*). Note that this trend is observed for all $\epsilon$ as shown in figures 4$(b, c)$. Qualitatively this can be seen in the midplane contour plots of the temperature which show the progression from a 'diffusive cloud' for low Reynolds numbers (figure 3*b*), to the convection dominated flow shown in figure 3$(f)$. The difference to the potential flow work by Choi *et al.* (2005) is the formation of a recirculation region for a sufficiently high Reynolds number, which broadens the wake significantly. To highlight the flow features present, streamlines are also shown with the black and green streamlines indicating streamlines starting from in front of and behind the cylinder, respectively. The effect this recirculation region has on the local Nusselt number can be seen in figure 3$(e)$ where the local Nusselt number no longer decreases monotonically towards the rear stagnation point.

Two metrics used to characterise recirculation regions are the length of the midplane wake $L_v$ which is defined as the distance from the rear stagnation point to the stagnation point in the wake and $\theta_v$ the midplane separation angle (measured from the rear stagnation point as seen in figure 1) which is the angle where the wall shear stress is zero. In figure 5$(a, b)$ the metrics from the present numerical simulations are compared against the two-dimensional numerical simulations from Rajani *et al.* (2009) and the experimental data from Coutanceau & Bouard (1977) which are only in the steady flow regime (up to $\bar{Re} \approx 50$). For $L_v$, a linear increase was found but with a milder slope (than the two-dimensional case) and the slope also decreases for decreasing $\epsilon$. Similarly for $\theta_v$, the trend is shifted to higher Reynolds numbers for increasing $\epsilon$. Note that for $\epsilon = 0.25$, no recirculation regions were present for the Reynolds numbers investigated.

### *4.2. Variation with $\epsilon$*

To show the effect of varying $\epsilon$, the data in figure 2 has been replotted in figure 6. For low Reynolds numbers, figure 6 shows that the Nusselt number for all the cases is approximately constant, which is to be anticipated as the system is diffusion dominated ($\bar{Pe} \approx 0.5$). To investigate the effect of decreasing $\epsilon$ and keeping $\bar{Re}$ constant, on the Nusselt number, the case of air and $\bar{Re} = 53.3$ is chosen. The azimuthal variation of the midplane local Nusselt number for $\epsilon = 1$ and 0.25 are plotted in figure 7$(a)$ which shows that there is a greater transfer at the front stagnation point for $\epsilon = 1$ but a lower transfer towards the rear of the cylinder. Figure 7$(b)$ shows the variation of the horizontal velocity and temperature on the midplane front stagnation point line and it can be seen that the horizontal velocity is greater (on

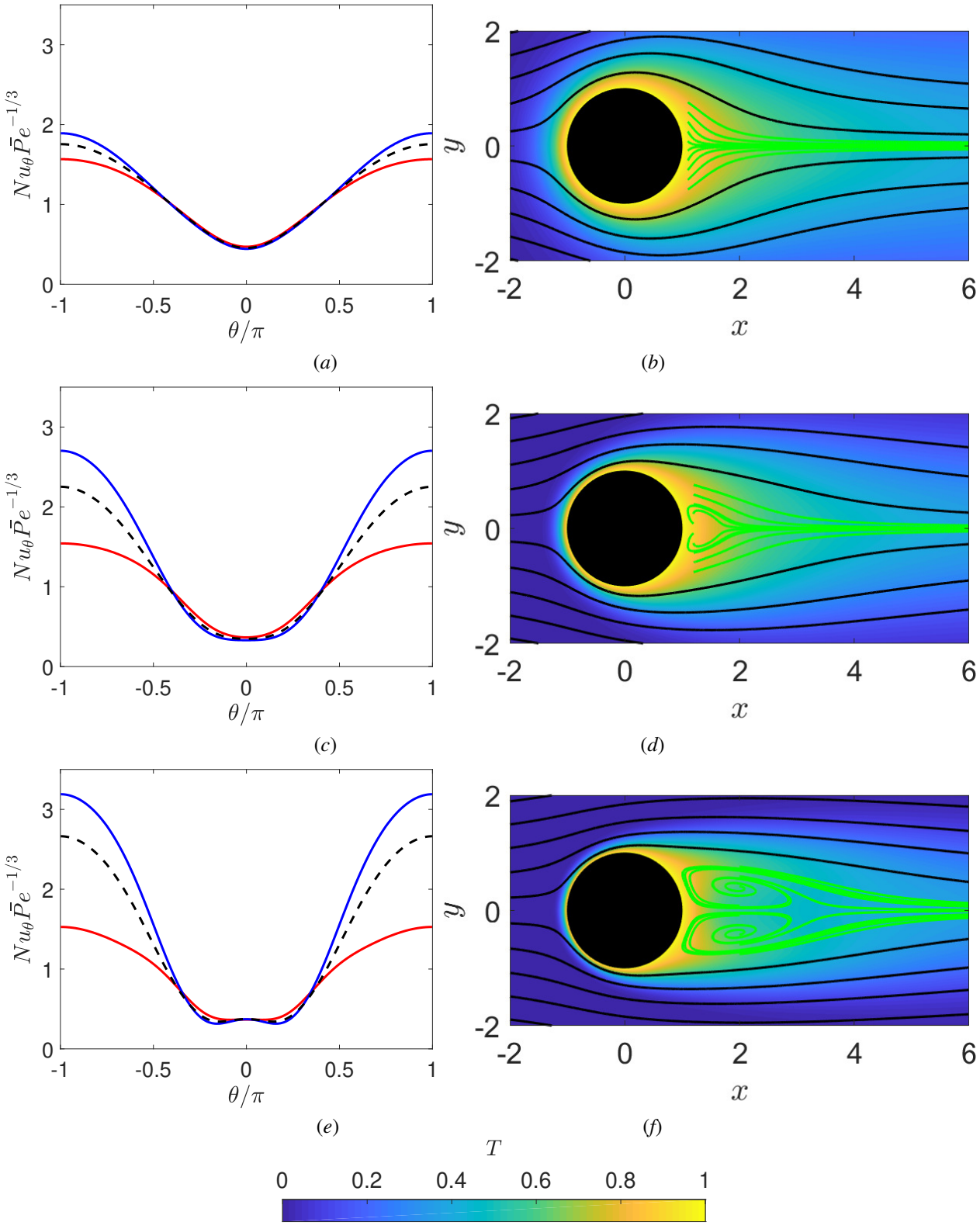


Figure 3: The $(a, c, e)$ variation of the local Nusselt number (at different elevations) and $(b, d, f)$ contour plots of the midplane temperature are shown respectively for air for $\epsilon = 1$ and $\bar{Re} = (a, b)$ 13.3, $(c, d)$ 53.3 and $(e, f)$ 106.7. The lines in $(a, c, e)$ represent $z^* = 0$ (blue lines) and $z^* = 0.87$ (red lines) while the black dashed lines are the average local Nusselt number. In $(b, d, f)$ streamlines, are shown in black and green, originating from in front of and behind the cylinder, respectively.

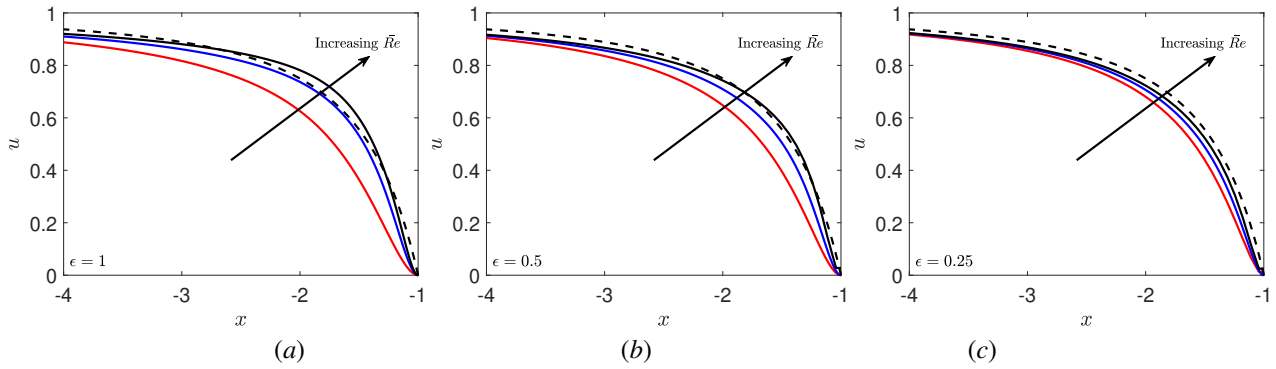


Figure 4: Midplane horizontal velocity variation on the front stagnation line for (*a*) $\epsilon = 1$, (*b*) $\epsilon = 0.5$ and (*c*) $\epsilon = 0.25$ for $\bar{Re} = 13.3$ (red line), 53.3 (blue line) and 106.6 (black line). The two-dimensional unbounded irrotational velocity profile for flow towards a circular cylinder is shown in a dashed black line.

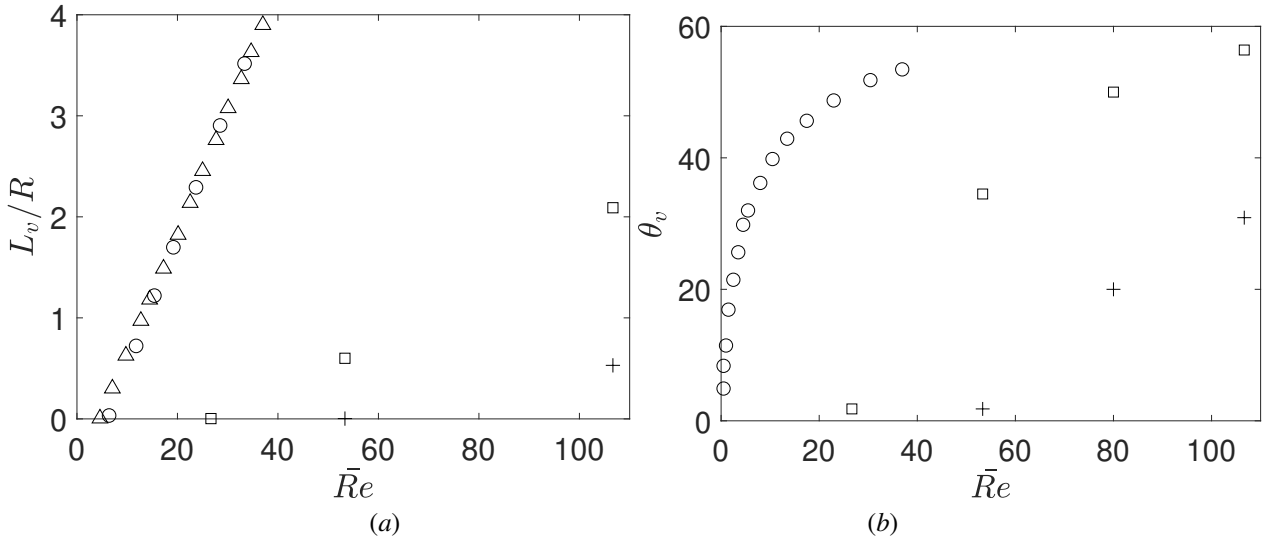


Figure 5: Variation of the (*a*) midplane length of the recirculation region and (*b*) the separation angle for different Reynolds numbers and vertical confinement. The current numerical simulations are shown for $\epsilon = 1$ (□) and $\epsilon = 0.5$ (+). The other symbols represent the experiments by Coutanceau & Bouard (1977) (△) and two-dimensional simulations by Rajani *et al.* (2009) (○).

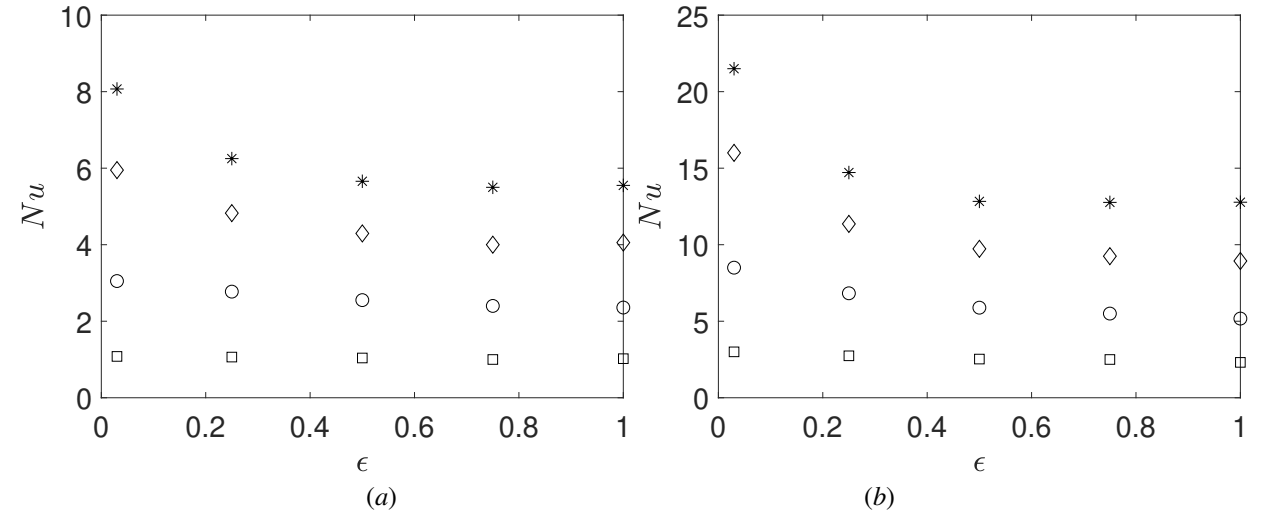


Figure 6: Variation of the Nusselt number with $\epsilon$ for (*a*) air and (*b*) water for different Reynolds numbers, $\bar{Re} = 0.67$ (□), 13.3 (○), 53.3 (⋄) and 106.7 (*).

approach to the cylinder) for $\epsilon = 1$ leading to a higher gradient in the temperature at the front stagnation point. Towards the rear of the cylinder the radial variation of the midplane temperature at $\theta = \pi/4$ is plotted in figure 7($c$), together with the tangential velocity. For $\epsilon = 0.25$ the gradient of the velocity is much steeper than for $\epsilon = 1$ as there is a recirculation region present for $\epsilon = 1$ (see figure 3$d$). Hence there is a steeper gradient in the temperature here and a higher transfer at the rear of the cylinder for $\epsilon = 0.25$. The integral effect is a greater transfer for $\epsilon = 0.25$. To investigate the effect of reducing $\epsilon$ further, a study of $\epsilon = 0.03$ will be presented.

## 5. Variation of $\Lambda$ and $Pe$ for $\epsilon = 0.03$

In this section the effect of varying $\Lambda$ and $Pe$ on the Nusselt number will be presented, while keeping $\epsilon = 0.03$. These trends are then analysed further by considering the variation of the local transfer in the azimuthal and vertical directions on the cylinder surface. The variation of the local Nusselt number are then explained by studying the structure of the flow-field, particularly the secondary flow induced adjacent to the cylinder at increased $\Lambda$. Note that these secondary flows only occur for $\epsilon \leq 0.5$ at sufficiently high $\Lambda$.

### 5.1. Nusselt number

In figure 8, the variation of the Nusselt number with $\Lambda$ and $Pe$ are shown. As $\Lambda$ is increased to approximately unity (and the Péclet number is in the range $1 < Pe \leq 10^3$), the Nusselt number does not significantly increase. A measure of the thermal boundary layer thickness $\delta_\alpha \sim RPe^{-1/2}$ and for the geometric boundary layer thickness is $\delta_g \sim R\epsilon$ such that $\delta_g/\delta_\alpha \sim \epsilon Pe^{1/2}$. Therefore if $Pe$ and $\epsilon$ is fixed, then increasing inertia ($\Lambda$) will not affect the thickness of either the thermal or the geometric boundary layer thickness, or the resulting transfer. As will be shown in the subsequent analysis, inertia plays a role in generating a secondary flow within the geometric boundary layer when $\Lambda$ is increased past $O(\epsilon)$, which does affect the transfer. For $\Lambda = 5$ there is a slight increase in the Nusselt number for all $Pe$ considered.

### 5.2. Local Nusselt number for $\Lambda \ll 1$ and $Pe \leq 10^2$

The variation of the local Nusselt number around the cylinder is shown in figure 9. To highlight the vertical variation, the blue line is the midplane transfer, the red line is the transfer close to the side walls ($z^* = 0.87$) and the dashed line is the depth-averaged local Nusselt number. In figure 9($a, d, g$) the local Nusselt number for $\Lambda = 10^{-3}, 1, 5$ for Péclet number of 1.1-111 are shown respectively. There is no vertical variation in the local Nusselt number for this range of $\Lambda$ and $Pe$. As is to be anticipated the highest surface flux is from the front stagnation point and this decreases with distance along the cylinder. However in figures 9($b, c$), the inertial parameter has been kept constant at $\Lambda = 10^{-3}$ and these show a vertical variation in the local Nusselt number as the Péclet number has been increased from $10^3$ to $10^4$. The local Nusselt number is greater at the midplane than at $z^* = 0.87$ which is due to the increased convection at the midplane (while simultaneously diffusive effects being stronger closer to the side walls) resulting in a thinner thermal boundary layer (at the midplane). With azimuthal distance from the front stagnation point, cross stream diffusion results in the local Nusselt number being equal downstream of the front stagnation point; this occurs at $\theta/\pi = 1/2$ (for $Pe = 1.1 \times 10^3$) and $\theta/\pi = 1/4$ (for $Pe = 1.1 \times 10^4$).

### 5.3. Local Nusselt number for $\Lambda \geq 1$ and $Pe \geq 10^3$

In the following discussion only numerical simulations for $Pe = 1.1 \times 10^4$ will be described, although the trends are similar for $Pe = 1.1 \times 10^3$. When $\Lambda$ is increased from $10^{-3}$ to 5 and $Pe = 1.1 \times 10^4$ the flux is increasingly higher in the midplane (than close to the side walls), at the front stagnation point (figure 9 $c, f, i$). Figure 10 shows midplane radial velocity and temperature profiles close to the front stagnation point. As $\Lambda$ increases the radial velocity decelerates closer to the circular cylinder resulting in an increased convection of the temperature towards the cylinder boundary, leading to a thinner thermal boundary layer (figure 10$b$) and an increased flux.

For $\Lambda \geq 1$ and $Pe = 1.1 \times 10^4$ the flux drops significantly in the midplane with azimuthal distance around the cylinder (away from the front stagnation point) while it increases close to the side walls (figure 9$f, i$). To show why this development occurs contour plots of the temperature in planes normal to the cylinder surface ($z^*$-$r^*$) are shown at four different angles between $1 > \theta/\pi > 1/2$ in figure 11($e$-$h$). Therefore although the boundary layer thickness does not change significantly, the effect of inertia is to set up a secondary flow within the boundary layer. This secondary flow at higher $\Lambda$, due to increased centrifugal forces in the midplane, results in two counter rotating vortices forming adjacent to the circular cylinder. Streamline plots in planes perpendicular to the cylinder surface (using $u_r$ and $u_z$) are shown in figure 11($f, g$). Close to the cylinder, on the windward side, the radial velocity has a triple turning point structure, with a radial outward flow in the midplane and a radial inflow close to the sidewalls. As $\Lambda$ increases this velocity profile becomes more pronounced; figure 12 shows vertical profiles of the radial velocity at $r^* = 1$ for increasing $\Lambda$. These contour plots also show how this azimuthally developing secondary flow affects the transfer. The radial velocity field then results in an increased convection of the temperature away and toward the cylinder surface in the midplane and close to the side walls, respectively. The modification of the temperature boundary layers can be seen in figure 11($e$-$h$) for $\Lambda = 5$.

## 6. Conclusions

This work has studied the forced convection past a circular cylinder in a planar Poiseuille flow for varying $Pe$ and $\Lambda$ for $0.25 \leq \epsilon \leq 1$ and $\epsilon = 0.03$. For $0.25 \leq \epsilon \leq 1$, for certain ranges of the Reynolds number, the Nusselt number increased with decreasing $\epsilon$. This behaviour was explained with a combination of hydrodynamic and thermal diagnostics. Future work includes investigating increasing the Reynolds number such that there is vortex shedding from the cylinder and seeing the effect this has on the thermal transfer.

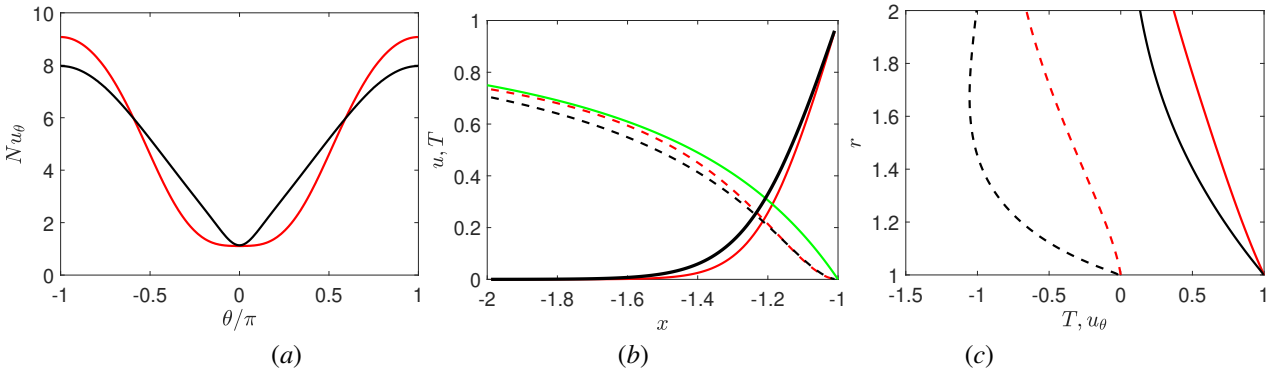


Figure 7: (*a*) Azimuthal variation of the midplane local Nusselt number for $\epsilon = 1$ (red line) and $\epsilon = 0.25$ (black line). (*b*) Streamwise variation of the temperature for $\epsilon = 1$ (red line) and $\epsilon = 0.25$ (black line) and horizontal velocity for $\epsilon = 1$ (red dashed line) and $\epsilon = 0.25$ (black dashed line) on the midplane front stagnation line (*i.e.* $\theta = \pi$). The potential flow solution is shown with a green line. (*c*) Radial midplane variation of the temperature for $\epsilon = 1$ (red line) and $\epsilon = 0.25$ (black line) and horizontal velocity for $\epsilon = 1$ (red dashed line) and $\epsilon = 0.25$ (black dashed line) at $\theta = \pi/4$. All data for air and $\bar{R}e = 53.3$.

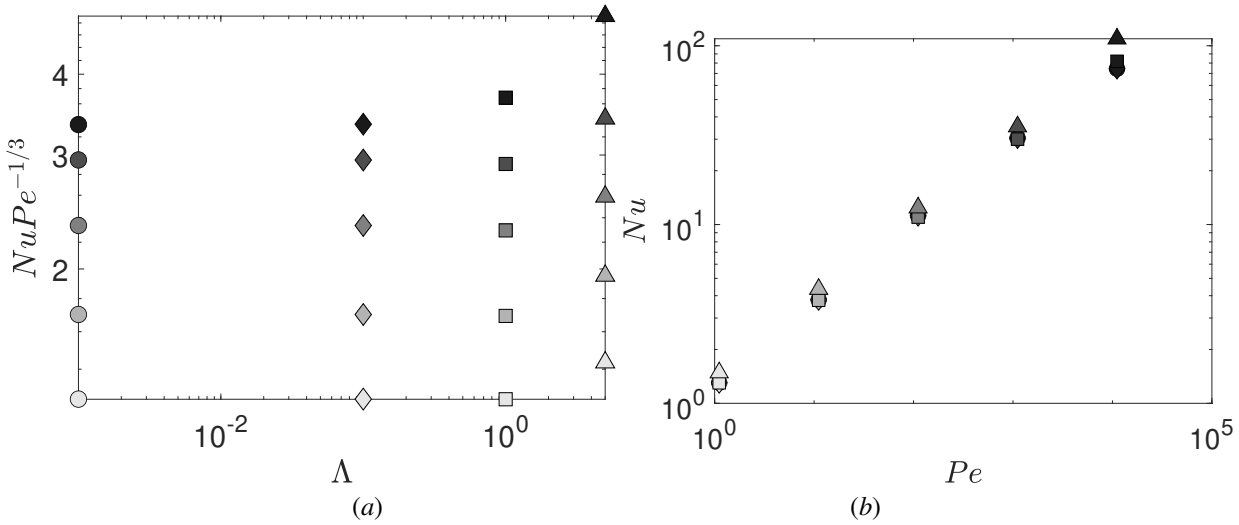


Figure 8: The variation of the Nusselt number with (*a*) $\Lambda$ and (*b*) *Pe* for $\Lambda = 10^{-3}$ (○), 0.1 (⋄), 1 (□) and 5 (△). *Pe* is increased from 1.1 to $1.1\times10^4$ (a darker symbol indicates a higher *Pe*).

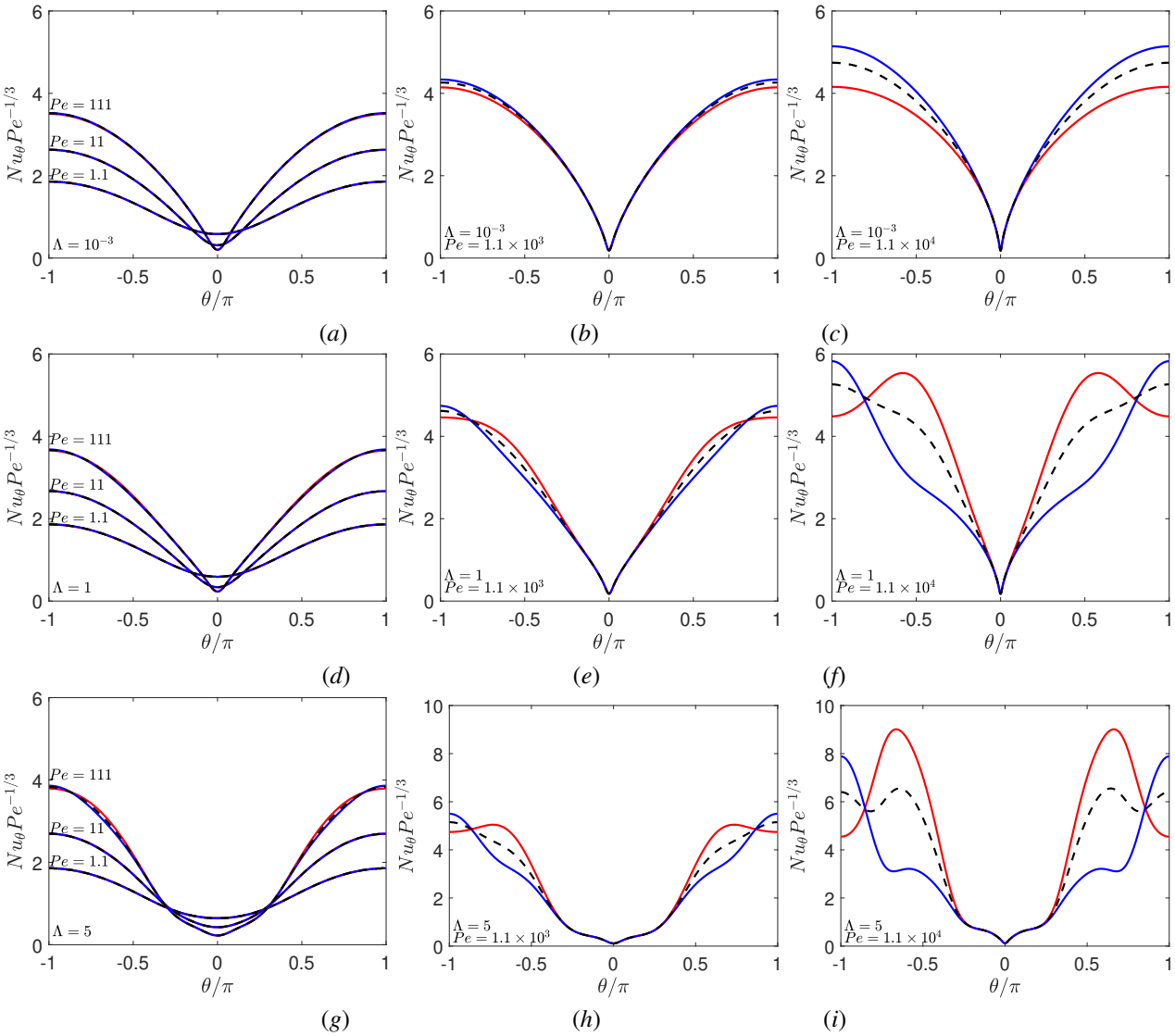


Figure 9: Azimuthal profiles of the local Nusselt number for different $Pe$ and $\Lambda = 10^{-3}$ for $(a, b, c)$, 1 for $(d, e, f)$ and 5 for $(g, h, i)$, at a vertical height $z^* = 0$ (blue lines) and $z^* = 0.87$ (red lines). The dashed lines are the average local Nusselt number.

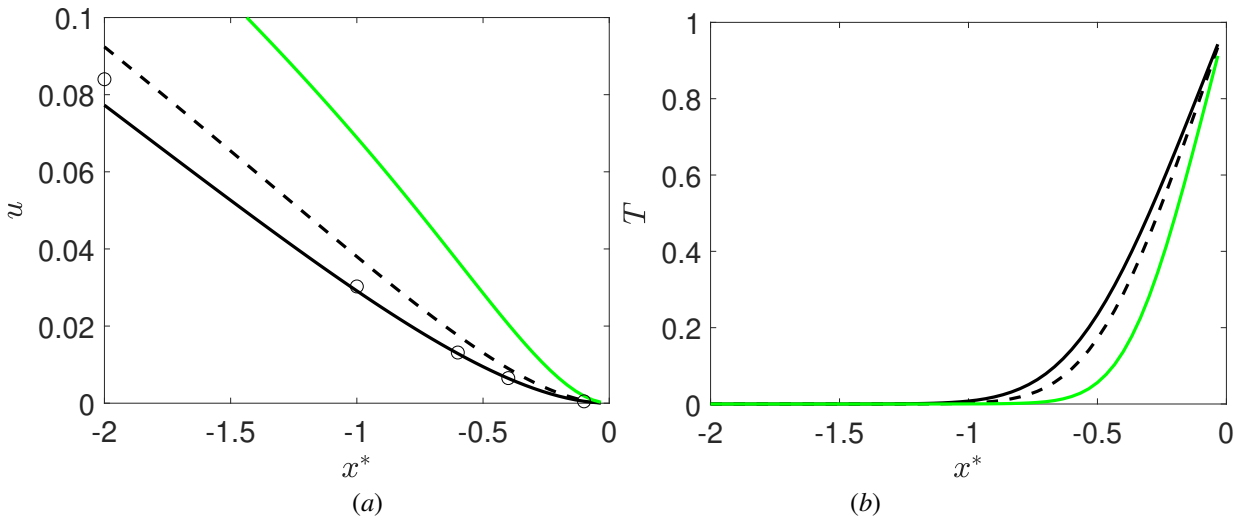


Figure 10: $(a)$ Midplane radial velocity and $(b)$ temperature profile at $\theta/\pi = 1$ for $Pe = 1.1 \times 10^4$ for $\Lambda = 10^{-3}$ (black lines), 1 (black dashed lines) and 5 (green lines). Thompson's (1968) numerical calculations are shown in ($\circ$).

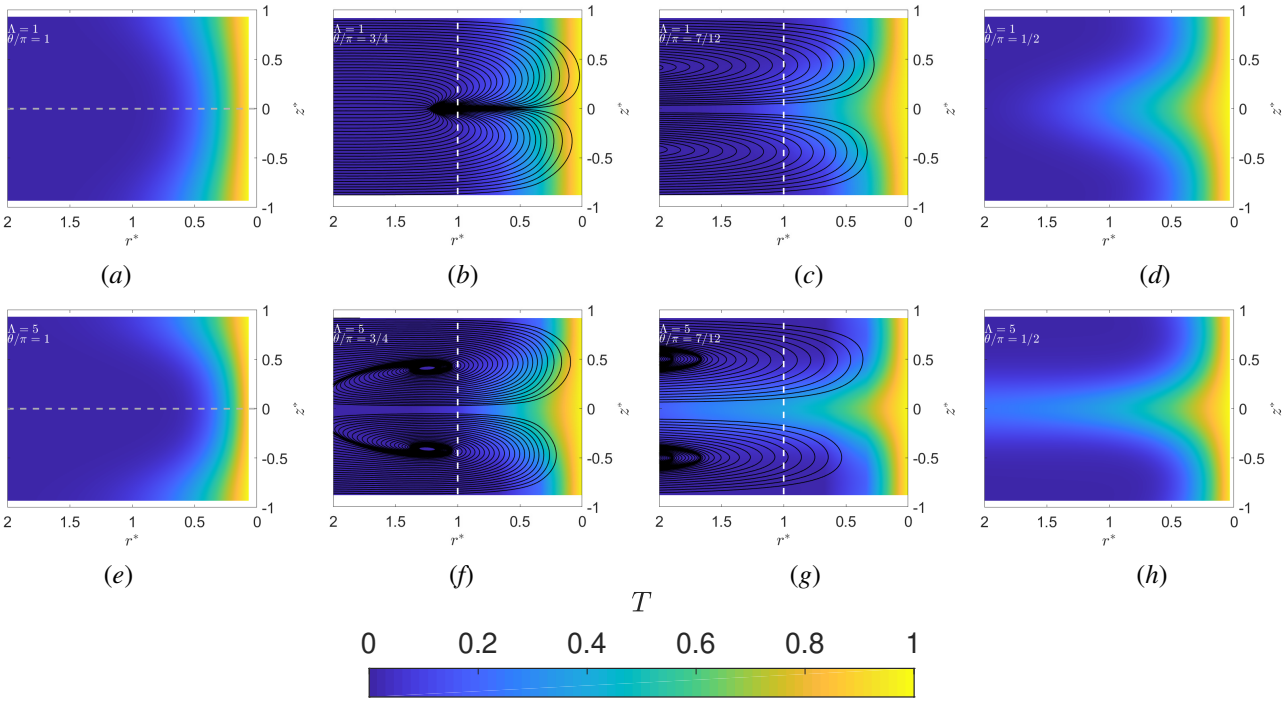


Figure 11: A contour plot of the temperature in planes normal to the cylinder surface ($z^*$-$r^*$) for $Pe = 1.1 \times 10^4$ and $\Lambda = 1$ for ($a$-$d$) and 5 for ($e$-$h$) and $\theta/\pi = 1$ for ($a, e$), 3/4 for ($b, f$), 7/12 for ($c, g$) and 1/2 for ($d, h$). In ($b, c, f, g$) the streamlines show the structure of the secondary flow. The horizontal dashed grey lines are the midplane profiles shown in figure 10 while the vertical dashed white lines are the vertical profiles shown in figure 12.

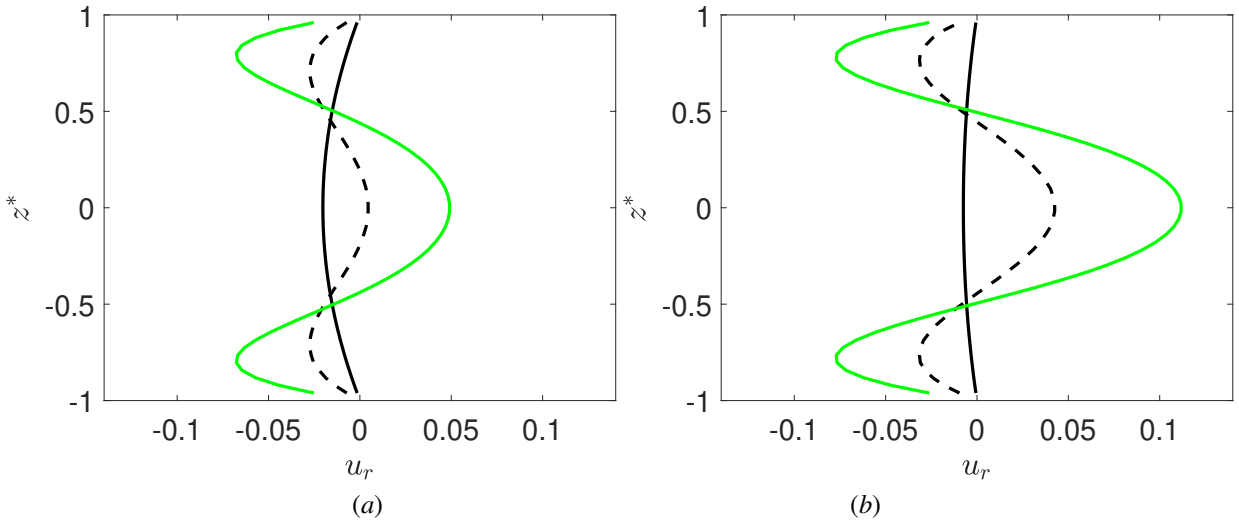


Figure 12: Vertical profiles of the radial velocity for $Pe = 1.1 \times 10^4$ at $r^* = 1$ and $\theta/\pi =$ ($a$) 3/4 and ($b$) 7/12 for $\Lambda = 10^{-3}$ (black lines), 1 (black dashed lines) and 5 (green lines).

For $\epsilon = 0.03$, it is found that for low $Pe$, the local Nusselt number is not sensitive to an increase in $\Lambda$ up to $O(1)$. If $\Lambda \ll 1$, a vertical variation of the local Nusselt number is present at the front stagnation point for $Pe \geq 10^3$, which is due to the non-uniform incident flow. The secondary flow, starting at $\Lambda = O(\epsilon)$, results in a radial velocity profile with a triple turning point, such that there is a thicker and thinner thermal boundary layer in the midplane and close to the sides, respectively. The surface flux then is significantly increased at the side walls compared to the midplane.


## Acknowledgements

The author acknowledges the use of the UCL's Myriad High Performance Computing Facility (Myriad@UCL) and Kathleen High Performance Computing Facility (Kathleen@UCL), and associated support services, in the completion of this work. The author thanks the two anonymous referees and the associate editor for helpful comments.


## Appendix A

These three-dimensional simulations require there to be a mesh independence in the $r$, $\theta$ and $z$ directions, which this appendix will document. The most sensitive geometry and flow parameters that were studied was for $\epsilon = 0.03$ (thin geometric boundary layer), $\Lambda = 5$ (high inertia resulting in a thin temperature boundary layer at the midplane front stagnation point) and $Pe = 1.1 \times 10^4$ (thin temperature boundary layer) and so a mesh independence study will be shown for this setup. The metric of interest that will be used is the local Nusselt number, which is appropriate as it is the diagnostic used frequently in the work and also is a function of the gradient of a temperature, and so, is sensitive to the mesh resolution. It is found that the variation in the azimuthal direction is not as significant as the variation in $r$ and $z$, so the focus will be on these two directions. Figure 13($a$) shows the effect of varying the radial resolution close of the cylinder from $\Delta_r/h = 2/21$ to $\Delta_r/h = 51$. There is little variation of the local Nusselt number and the Nusselt number of the three cases is within 1%. Figure 13($b$) shows the effect of varying the vertical resolution. It can be seen that the vertical variation is more sensitive than the radial direction and requires a finer mesh. Close agreement between all the meshes was also found for these cases.

## References


[1] Batchelor, G.K. 1967 *An Introduction to Fluid Dynamics*, 1st edn. Cambridge University Press.

[2] Choi, J., Margetis, D., Squires, T.D. & Bazant, M.Z. 2005 Steady advection-diffusion around finite absorbers in two-dimensional potential flows. *J. Fluid. Mech.* **536**, 155–184.

[3] Churchill, S.W. & Bernstein, M.J. 1977 A correlating equation for forced convection from gases and liquids to a circular cylinder in crossflow. *J. Heat Mass Trans.* **99**, 300–306.

[4] Coutanceau, M. & Bouard, R. 1977 Experimental determination of the main features of the viscous flow in the wake of a circular cylinder in uniform translation: steady flow. *J. Fluid. Mech.* **70**, 231–256.

[5] Dennis, S.C.R., Hudson, J.D. & Smith, N. 1968 Steady laminar forced convection from a circular cylinder at low Reynolds numbers. *Phys. Fluids* **11**, 933–940.

[6] Gorin, A.V., Zarubin, A.V., Mikhailova, T.N., Muhkin, V.A. & Sikovskii, D.F. 1995 Friction and mass transfer in transverse flow around a cylinder in a granular bed and a narrow slot. *J. Appl. Mech. Tech. Phys.* **36**, 105–113.

[7] Guglielmini, L., Rusconi, R., Lecuyer, S. & Stone, H.A. 2011 Three-dimensional features in low-Reynolds-number confined corner flows. *J. Fluid. Mech.* **668**, 33–57.

[8] Klettner, C.A. 2020 Transfer and Transport of a passive scalar within an isolated array of circular cylinders in a uniform flow. *Water Res. Res.* 56(9), e2020WR027618.

[9] Klettner, C.A. & Smith, F.T. 2022 The effect of inertia and vertical confinement on the flow past a circular cylinder in a Hele-Shaw cell. *J. Fluid Mech.* **934**, A8. doi:10.1017/jfm.2021.1128

[10] Knudsen, J.D. & Katz, D.L. 1958 Fluid dynamics and heat transfer. New York: McGraw Hill.

[11] Ladd, A.J.C., Yu, L. & Szymczak, P. 2020 Dissolution of a cylindrical disk in Hele-Shaw flow: a conformal mapping approach. *J. Fluid. Mech.* **903**, A46. doi:10.1017/jfm.2020.609

[12] Mahir, N. & Altac, Z. 2014 Numerical investigation of convective heat transfer in unsteady flow past two cylinders in tandem arrangements. *Int. J. Heat Fluid Flow.* **29**, 1309–1318.

[13] Rajani, B.N., Kandasamy, A. & Majumdar, S. 2009 Numerical simulation of laminar flow past a circular cylinder. *Appl. Math. Modelling.* **33**, 1228–1247.

[14] Renfer, A., Tiwari, M.K., Tiwari, R., Alfieri, F., Brunschwiler, T., Michel, B. & Poulikakos, D. 2013 Microvortex-enhanced heat transfer in 3D-integrated liquid cooling of electronic chip stacks. *Int. J. Heat Fluid Flow.* **65**, 33–43.

[15] Thompson, B.W. 1968 Secondary flow in a Hele-Shaw cell. *J. Fluid. Mech.* **31**, 379–395.

[16] Tuckerman, L.S., Kreilos, T., Schrobsdorff, H., Schneider, T.M. & Gibson, J.F. 2014 Turbulent-laminar patterns in plane Poiseuille flow. *Phys. Fluids.* **26**, 114103.

[17] Weller, H.G., Tabor, G., Jasak, H. & Fureby, C. 1998 A tensorial approach to computational continuum mechanics using object-oriented techniques. *Comput. Phys.* **12**, 620–631.

[18] Zdrakovich, M.M. 1997 Flow around circular cylinders: applications Vol. 1. Oxford University Press.

[19] Zhang, S., Cagney, N., Balabani, S., Naveira-Cotta, C.P. & Tiwari, M.K. 2019 Probing vortex-shedding at high ferquencies in flows past confined microfluidic cylinders using high-speed microscale particle image velocimetry. *Phys. Fluids.* **31**, 102001.

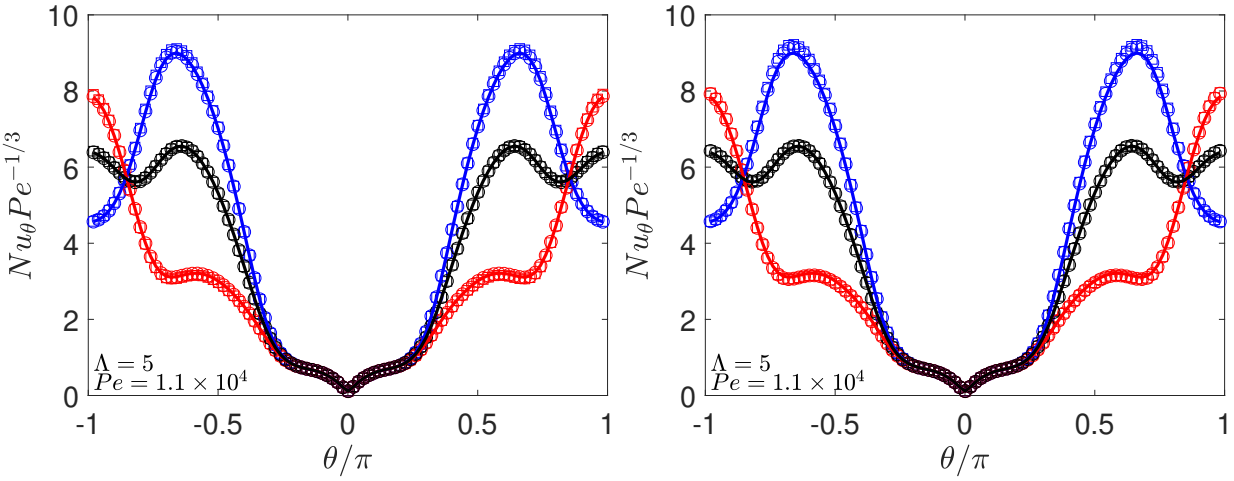


Figure 13: Azimuthal profiles of the local Nusselt number for $\epsilon = 0.03$, $Pe = 1.1 \times 10^4$ and $\Lambda = 5$ for the (*a*) radial and (*b*) vertical mesh independence study. Shown are the average local Nusselt number (black symbols), $z^* = 0$ (blue symbols) and $z^* = 0.87$ (red symbols). In (*a*) the symbols represent $\Delta_r/h$ = 2/21 (□), 2/31 (∘) and 2/51 (lines). In (*b*) the lines represent $\Delta_z/h$ = 2/21 (□), 2/51 (∘) and 2/71 (lines).